MilliSign: mmWave-Based Passive Signs for Guiding UAVs in Poor Visibility Conditions

Tatsuya Iizuka[1,2], Takuya Sasatani[2], Toru Nakamura[1],
Naoko Kosaka[1], Masaki Hisada[1], Yoshihiro Kawahara[2]
[1]Nippon Telegraph and Telephone Corporation, Tokyo, Japan
[2]The University of Tokyo, Tokyo, Japan

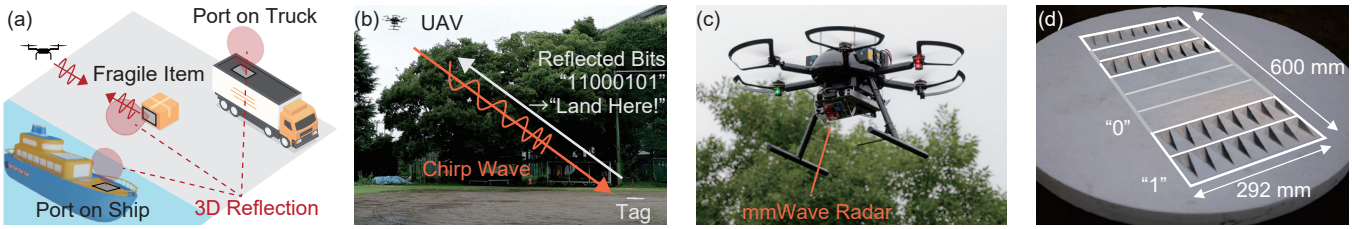

Figure 1: An overview of MilliSign, a passive sign-to-UAV communication system based on spatial coding-chipless RFID technology and off-the-shelf mmWave radars. (a) Application scenarios of MilliSign. (b) Slant range readout procedure from the UAV. (c) mmWave radar mounted on the UAV. (d) Our developed tag encoding "11000101."

ABSTRACT

This paper presents MilliSign, a guidance system based on a batteryless tag to support unmanned aerial vehicles in all-weather conditions. Conventional batteryless guidance systems using visual signs fail to work in inclement weather due to poor visibility. The need for all-weather operation with long-range readability encourages the use of millimeter wave (mmWave) radar, which poses challenges in providing a wide 3-D read range and low-cost operation. To address these challenges, we introduce a corner reflector (CR) array-based chipless RFID tag and a one-shot slant range reading procedure with COTS mmWave radar. We establish a novel design method for the shape and alignment of CR units to decrease the tag's size and expand the 3-D read range. Additionally, we develop a signal-processing pipeline based on Root-MUSIC to achieve accurate power and spatial estimation, which facilitate automatic tag detection. Our evaluation demonstrates that the tag, measuring 292 mm × 600 mm × 19 mm and storing 8 bits, can be read by mmWave radar from a distance of more than 10 m with a viewing angle of more than 30° in elevation and azimuth. Moreover, its performance remains stable in poor visibility conditions and multipath-rich environments.

CCS CONCEPTS

• **Hardware → Sensor applications and deployments**.

KEYWORDS

Chipless RFID, Millimeter wave radar, UAV

ACM Reference Format:
Tatsuya Iizuka[1,2], Takuya Sasatani[2], Toru Nakamura[1], Naoko Kosaka[1], Masaki Hisada[1], Yoshihiro Kawahara[2]. 2023. MilliSign: mmWave-Based Passive Signs for Guiding UAVs in Poor Visibility Conditions. In *The 29th Annual International Conference on Mobile Computing and Networking (ACM MobiCom '23), October 2–6, 2023, Madrid, Spain.* ACM, New York, NY, USA, 15 pages. https://doi.org/10.1145/3570361.3613264

1 INTRODUCTION

Unmanned aerial vehicles (UAVs) can perform complex tasks in hard-to-reach places, making them a promising technology to serve as a future infrastructure by automating various outdoor tasks in fields such as logistics [42], environmental monitoring [22, 24, 29], agriculture [46], disaster monitoring [14], and facility inspection [27]. As we move toward this future, UAVs are required to perform advanced tasks that demand flight control capabilities based on the local context in addition to global coordinates in GNSS systems such as

ACM MobiCom '23, October 2–6, 2023, Madrid, Spain

ACM ISBN 978-1-4503-9990-6/23/10.
https://doi.org/10.1145/3570361.3613264

RTK [17]. For instance, UAVs must be able to recognize the type of cargo they are carrying and carefully deliver fragile items to trucks, or autonomously land on the deck of a ship once their atmospheric observation task over the ocean is complete. Such functions basically rely on cameras to read conventional visual tags such as barcodes and alcomarkers, which guide UAVs with supportive information embedded. However, relying on cameras directly creates problems in inclement weather (*e.g.*, heavy rain) or at nighttime due to poor visibility. In practice, UAVs flying in such conditions are strictly limited by law due to the risk of incorrect flight control [34]. Therefore, guidance tags that can be read even in poor visibility conditions would enable UAVs to perform advanced missions under all-day and all-weather conditions in order to fully realize their potential as infrastructure.

The need for all-weather operation encourages the use of mmWave radars as reader devices, as automobiles have equipped them for recognizing vehicular spacing with all-weather tolerance. When designing tags to support UAV missions in locations with a high cost of access, such as urban high-altitude buildings and marine and mountainous regions, the tags must be batteryless to reduce maintenance cost. For vehicles on the ground, batteryless tags based on mmWave radars have performed roadside-to-vehicle communication [33]. These tags, which use 2-D retroreflectors called Van Atta array antennas and spatial chipless RFID techniques, can be read out as a bit sequence by a passing radar using synthetic aperture radar (SAR). However, these techniques cannot be applied to UAVs, which have a 3-D operating range and short operation time due to strictly limited battery capacity. Specifically, tags consisting of a Van Atta array antenna do not have a wide 3-D read range property, and SAR cannot achieve high-resolution readout and localization by a one-shot measurement.

This paper presents MilliSign, a passive sign-to-UAV communication system that (i) operates in all-weather conditions, (ii) works with batteryless tags, (iii) offers a wide 3-D read range, and (iv) achieves localization with a one-shot readout. As shown in Figure 1, our system employs CR array-based chipless RFID tags to achieve a wide 3-D read range. It also uses slant range reading methodology to enable one-shot readout and localization with COTS mmWave frequency-modulated continuous-wave (FMCW) radar. While numerous research efforts have been conducted in the domain of UAV navigation, none have achieved all these requirements simultaneously. Our approach includes significant inventions in tag design and radar signal processing, resulting in a compact tag size, scalable read range, and robust readout performance for varying UAV positions and in multipath-rich environments. This work makes two technical contributions:

Corner Reflector Array-Based Chipless RFID: The first invention establishes a new design method for a compact corner reflector-based spatial domain chipless RFID that provides a wide 3-D read range. Compared to previous methods using the Van Atta array antenna, the corner reflector has a larger unit structure, making the entire tag too large to create a bit array. Furthermore, ordinary corner reflectors have fixed angular characteristics, which limit the range of readings from the air. To address these issues, we developed a tag design method with the shape and alignment of CR unit that makes the overall tag size compact while enabling the design of the readable range in terms of distance and angle. This has resulted in a tag measuring 300 mm × 600 mm × 19 mm and storing 8 bits that can be read by COTS mmWave radar from a distance of more than 10 m with a viewing angle of more than 30° in elevation and azimuth.

Root-MUSIC-based Automatic Tag Detection: The second invention is a signal-processing method for the automatic detection and reading of our tags in a real environment with high accuracy, using the Root-MUSIC method and DBSCAN. Conventional FFT-based signal processing methods face limitations in accurately capturing a sequence of reflectors, as their intervals vary with the look angle or mid-air position, while FFT-based methods have fixed spatial resolution. This often results in readout failures with UAVs that move around in the air. To overcome this limitation, we developed a signal processing pipeline based on the Root-MUSIC method. By calculating corresponding eigenvalues (roots) over a wide 3-D area, this method can accurately output spatial positions and the received power of reflectors as roots. Further, taking advantage of the fact that our tag has the same level of power and spatial proximity in reflection, we implemented an automatic tag detection using DBSCAN [15] by clustering the point cloud (roots) based on distances in 4-D space consisting of the power (1-D) and position (3-D). Our method shows robust detection and readout capability of the tag, even in multipath-rich environments.

By combining these two developed techniques, we implemented MilliSign and evaluated it through intensive outdoor experiments. In summary, the contributions of this study are as follows:

- We design, implement, and evaluate MilliSign, a batteryless and all-weather guidance system for UAVs that offers a wide 3-D read range and one-shot readability.
- We establish a design method for a compact corner reflector-based spatial domain chipless RFID, which enables a wide 3-D readable area in terms of distance and angle.
- We develop a signal processing method that enables the automatic detection and readout of the tags with high accuracy in a real environment.

2 RELATED WORK

Our goal is to realize a UAV guidance system that meets the following requirements: (i) all-weather tolearance, (ii) batteryless tags, (iii) wide 3-D read range, and (iv) one-shot localization. To investigate the appropriate approach, we introduce a variety of related techniques.

Vision-Based Recognition: Optical sensors, such as cameras and LiDARs, have shown significant performance for UAV perception when combined with neural networks [1]. Simultaneous localization and mapping has received substantial research interest due to its centimeter accuracy [9]. Passive visible light communication was also investigated [50]. However, optical sensor recognition is sensitive to weather conditions due to the small wavelength (about 1 μm or less) of optical rays.

Sonar: Sonar sensors have strong permeability and are widely used for measuring surroundings, such as for collision detection [43] and fish finding [30]. However, the detection range of small ultrasonic sensors for UAVs is limited to about 1 m due to the low power of the speakers [35].

RFID: RFID technology is widely used in logistics and retail industries for inventory management. It can be read at up to 5 m using microwave interrogation and can encode over 1 kilobyte of information [49]. Thanks to intensive research and development, there are now many methods in the literature for localizing RFID tags using the principle of triangulation [18, 39]. However, quick localization for UAVs is challenging due to the need for multiple readouts for triangulation. Additionally, received signal strength indication-based range detection is typically inaccurate [31]. Furthermore, the antennas of RFID readers need to be large because the wavelength of the UHF band is 30 cm, and equipping such antennas on UAVs would constrain the payload.

Chipless RFID: Chipless RFID is a kind of bar code read by electromagnetic wave interrogation [5, 19, 28]. Tags encoded with electromagnetic characteristics are interrogated and interpreted by the reader as a bits pattern with different electromagnetic emissions. Three types of modulation schemes are commonly used: time-domain, frequency-domain, and spatial-domain. However, most chipless tags in the time and frequency domains have limited interrogation zones and operate in UHF bands, leading to larger systems.

Spatial Domain Chipless RFID: Spatial domain chipless RFID tags have been gaining attention, as improved electromagnetic imaging resolution brings high information density. SAR techniques are commonly used to read out spatial domain chipless tags with high resolution [3, 32, 37, 56], but this requires a series of measurements at different positions. mmWave-based communication and radar techniques have also been explored due to their low cost but high resolution [11, 25, 38, 47, 48, 54]. Side-looking radar in mmWave was introduced in [2], which showed high-resolution 2-D radar images in a laboratory environment. The results indicated that slant range reading with mmWave frequency offers not only enough information density but also a simple readout procedure. Therefore, we apply slant range reading and enhance its practicability by developing a signal-processing procedure.

Table 1: Comparison with related work.

Solution	All-weather tolerance	Batteryless tag	Wide 3-D read range	One-shot localization
Optics [1, 9]		✓	✓	✓
Sonars [35]	✓	✓		✓
RFID [18, 39]	✓	✓		
Millimetro [41]	✓			✓
RoS [33]	✓	✓		
MilliSign	✓	✓	✓	✓

Regarding the tag structure, the design of the scatterer element is crucial. The Van Atta array antenna structure, known for its retro-reflective principle and wide-range readability, has been widely employed in prior studies, such as those of RoS [33] and Millimetro [41], to enable a broad read-range for automobiles. However, the single-plane retro-reflective attributes of this structure cannot offer a 3-D wide read range, making it unsuitable for UAVs that operate in 3-D spaces. On the other hand, CR is a conventional high radar cross-section (RCS) scatterer with retro-reflective attributes for 3-D incident waves. While CR-based chipless RFID in the frequency domain has been proposed [8, 26], there have been no studies on CR-based chipless RFID with spatial modulation, which poses technical challenges in terms of its large size and the design of the 3-D read range.

Table 1 summarizes the work mentioned above with the requirements of the sign-to-UAV communication system. The absence of a technology that meets all these requirements motivated our study of MilliSign.

3 SYSTEM OVERVIEW

This section provides a system overview of the slant range readout process for UAVs. The system configuration and coordinates are shown in Figure 2. The system consists of tags installed on the ground and mmWave radars mounted on UAVs located in the air. The tag is located so that its first bit is located at the origin, and its bits are arranged along the x-axis in a negative direction.

3.1 Spatial Coding with Side-Looking Radar

CRs are distributed on a horizontally placed tag and encoded as a bit sequence. The side-looking radar, commonly used in satellite radar systems to investigate ground surfaces, can decode the tag by analyzing the range power profile. This

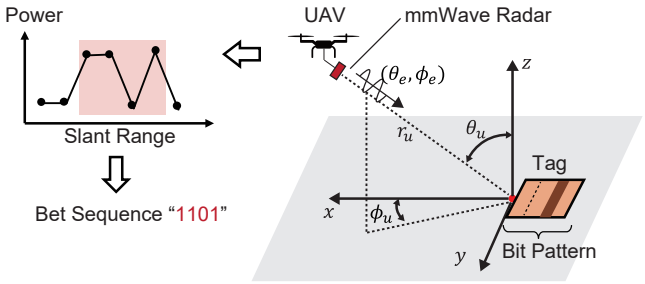

Figure 2: System configuration of MilliSign, to read out a spatial-domain chipless RFID tag with side-looking radar. The bits "1" or "0" can be decoded by the range power analysis at the radar position.

readout approach not only provides a simple one-shot readout procedure but also offers advantages over SAR-based readouts. Specifically, side-looking radar tends to achieve a high signal-to-noise ratio (SNR) due to the small backscattering RCS of outdoor surfaces such as terrain, roads, and the sea. Specular reflections result in low noise levels and facilitate extracting signals from CRs. Additionally, this approach facilitates installation, as it only requires the use of small, lightweight, and COTS mmWave radar sensors on UAVs.

A bit sequence can be encoded into a tag by CRs' arrangement pattern, designed as a black line alignment of bar codes. Since the readout accuracy and bit error rate are highly dependent on the SNR in chipless RFID [7], achieving a large difference in reflected power between bits "1" and "0" is crucial. To this end, a flat metal plane can serve as bit "0", since its backscattering RCS is low due to the principle of specular reflection. Thus, the bit sequence can be determined by the order in which the flat planes and CRs are placed.

3.2 Localization with MIMO Radar

COTS mmWave FMCW radar can localize the reflector in terms of distance, azimuth angle, and elevation angle. The distance estimation is achieved through the use of chirp waves, which convert the distance to a reflector into a frequency in an intermediate frequency (IF) signal. Range frequency analysis is conventionally performed using FFT, called range FFT. With MIMO radar, the angle of arrival can be estimated by analyzing the phase rotation that appears in multiple receiving antennas. This is achieved using the digital beamforming method, which provides an angle resolution of $1/n$, where n is the number of receiving antennas. Taking as an example a TI radar device with a carrier frequency $f_c = 79$ GHz, chirp bandwidth $B = 4.0$ GHz, and two horizontally aligned transmit antennas and four received antennas, the calculated distance resolution is 37.5 mm, and the horizontal angle resolution is 14°. While other signal processing techniques, such as MUSIC [52], can improve localization accuracy, the spatial resolution will not be significantly different.

4 PROBLEM STATEMENT

In this section, we present the signal model of reading chipless tags with FMCW radar mounted on UAVs leveraging the coordinate system illustrated in Figure 2. We then discuss the technical challenges in realizing the practical system.

4.1 Signal Model

4.1.1 Signal Intensity and Maximum Detectable Distance. The readout performance of a system, including its SNR, BER, and maximum detectable distance, depends on the signal strength from reflectors. Hence, modeling the received power P_r from a reflector placed at the origin is crucial in designing and optimizing the system. We define $\sigma(\theta, \phi)$ as the backscattering RCS of the reflector, $G(\theta, \phi)$ as the radar antenna gain, and $r_\mathrm{u}, \theta_\mathrm{u}, \phi_\mathrm{u}$ as the UAV's location in polar coordinates. We also assume fixed radar gain G and orientation $\theta_\mathrm{e}, \phi_\mathrm{e}$ in the study, assuming that the tag's position is unknown to the UAV and the UAV searches for the sign while facing the same direction. The received power P_r from one reflector is then formulated as follows [40]:

$$P_\mathrm{r}(\sigma, r_\mathrm{u}, \theta_\mathrm{u}, \phi_\mathrm{u}) = \frac{P_\mathrm{t}\lambda^2}{(4\pi)^3} \cdot \frac{G(\theta_\mathrm{u}+\theta_\mathrm{e}, \phi_\mathrm{u}+\phi_\mathrm{e})^2 \sigma(\theta_\mathrm{u}, \phi_\mathrm{u})}{r_\mathrm{u}^4}, \quad (1)$$

where P_t is the transmission power and λ is the wavelength of the carrier frequency. The maximum detectable distance R_max is calculated with minimum detectable power S_min as follows [40]:

$$R_\mathrm{max} = \left[\frac{P_\mathrm{t}\lambda^2 G(\theta_\mathrm{u}+\theta_\mathrm{e}, \phi_\mathrm{u}+\phi_\mathrm{e})^2 \sigma(\theta_\mathrm{u}, \phi_\mathrm{u})}{(4\pi)^3 S_\mathrm{min}} \right]^{\frac{1}{4}}. \quad (2)$$

4.1.2 Readout of Bits from Received Signal. The decoding of bit sequences involves processing reflected signals from multiple reflectors. To model the received signal, we define the number of bits as N, with the bit pattern represented by $b_\mathrm{n} = \{0, 1\}$, and the distance between reflectors as d_x. Additionally, we consider the backscattering RCS of bits "1" and "0" as $\sigma_1(\theta, \phi)$ and $\sigma_0(\theta, \phi)$, respectively. By arranging the corresponding bit reflectors along the x-axis with equal intervals, we can approximate the distance from the UAV to the n-th reflectors as $r_\mathrm{u} + n \cdot d_\mathrm{x} \sin\theta_\mathrm{u} \cos\phi_\mathrm{u}$, given that $r_\mathrm{u} \gg d_\mathrm{x}$. Then the received IF signal $s(t)$ is formulated as

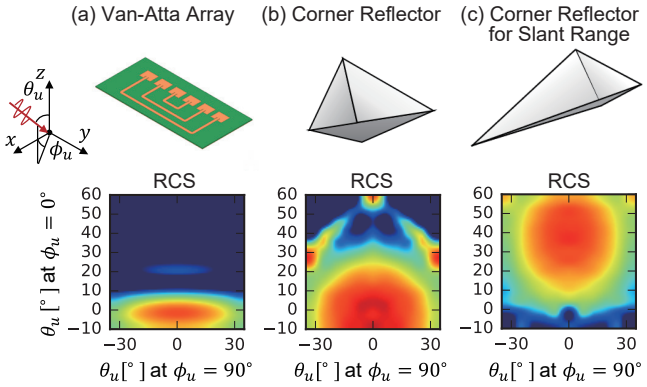

Figure 3: Backscattering RCS pattern of three reflector types with the same geometry surface area: (a) Van Atta array antenna, (b) conventional corner reflector, and (c) corner reflector optimized for slant range reading.

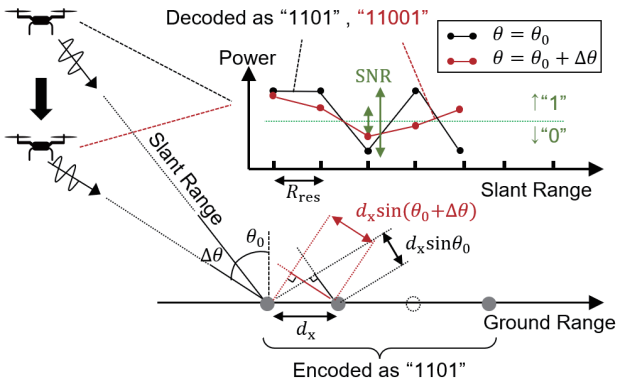

Figure 4: Difficulty in reading out bits with varying look angles. The obtained range power profile, along with the slant range, varies with look angle θ_u, causing the deterioration of SNR between bits "0" and "1."

$$s(t) = \sum_{n=1}^{N_x} c_n \cdot e^{j2\pi(f_s+nf_x)t} + w(t), \quad (3)$$

$$f_x = \frac{1}{T} \cdot \frac{d_x}{R_{res}} \sin\theta_u \cos\phi_u, \quad (4)$$

$$|c_n| = P_r^{\frac{1}{2}}(\sigma_b, r_u + n \cdot d_x, \theta_u, \phi_u), \quad (5)$$

$$\angle c_n = 2\pi j \frac{(r_u + n \cdot d_x \sin\theta_u \cos\phi_u)}{\lambda}, \quad (6)$$

$$\sigma_b = \begin{cases} \sigma_1(\theta_u, \phi_u) & (b_n = 1), \\ \sigma_0(\theta_u, \phi_u) & (b_n = 0), \end{cases} \quad (7)$$

where f_s is the intermediate frequency associated with the distance to the first-bit reflector, T is the time duration of the chirp signal, $R_{res} = c/2B$ is the distance resolution with standard range FFT, B is the chirp bandwidth, and c is the speed of light. R_{res} equals 37.5 mm with a 4 GHz bandwidth, which is a common configuration in 79 GHz mmWave FMCW radar. Although the angle resolution is not high enough to distinguish reflectors aligned perpendicular to the direction of arrival at intervals of several centimeters, as discussed in Section 3.2, bits can be read out when d_x is set as the same extent to R_{res}.

4.2 Technical Challenges

4.2.1 Compact Tag Size and Wide Read Range. As we model the signal readout process with 3-D polar coordinates, the reflector element can be evaluated by RCS $\sigma(\theta_u, \phi_u)$. While the Van Atta array has been widely adopted for its retroreflective structures and high RCS, it provides wide angular characteristics only for a single plane. In contrast, CR has extremely high RCS over three dimensions, making it an ideal candidate for wider 3-D reading. Figure 3 shows the backscattering RCS of the three reflector types with the same geometry surface area, calculated with HFSS, an electromagnetic fields simulator. As shown in Figure 3b, the conventional CR maintains the high RCS for incident waves with angles of $\theta_u < 30°$, limiting the 3-D read range in slant range reading scenarios. Furthermore, CRs are not suitable for alignment due to their 3-D geometry, making it difficult to encode bit patterns and leading to larger tag size.

To address these challenges, we investigate the shape of the CR unit to achieve compact yet high reflection for shallower directions. Figure 3c shows our optimized CR unit for slant range reading, maintaining the high RCS for $10° < \theta_u < 60°$. In Section 5, we present a CR array-based tag design method that enables a wide 3-D read range and describe the minimum size of CRs required to perform with retroreflection, reducing the tag size.

4.2.2 Accurate and Robust Readout of Bits. In the context of UAV communication, accurate decoding is critical to the system's performance. However, the conventional signal processing method of range FFT is limited by its fixed-range frequency resolution. By applying FFT to the time-domain beat signal, a power spectrum can be obtained as follows:

$$s(t) = \sum_{n=1}^{N} c_n \cdot e^{j2\pi n f_{res} t}, \quad (8)$$

$$f_{res} = \frac{1}{T}. \quad (9)$$

FFT analysis works well when the range frequency resolution f_{res} in Eq. 9 matches the frequency interval f_x in Eq. 4, which depends on the path difference and the look angles θ_u, ϕ_u. Thus, varying look angles can cause a mismatch between

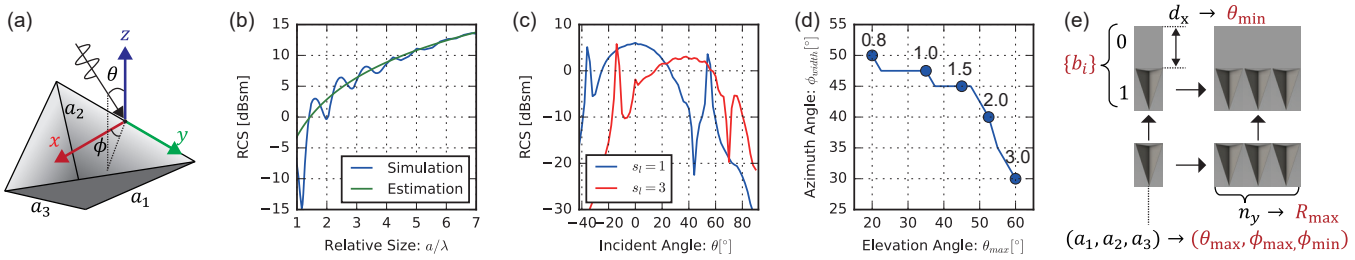

Figure 5: (a) Geometry of a CR and coordinates for angular characteristic evaluation. (b) RCS at carrier frequency $f_c = 79$ GHz and incident angle $\theta = 0°$ with varying length a ($a_1 = a_2 = a_3 = a$ in this simulation). (c) Example of the RCS angular characteristics variation by different edge length ratios $s_l = a_3/a_1$ ($a_1 = a_2$ in this study). (d) Tradeoff between θ_{max} and $\phi_{width} = \phi_{max} - \phi_{min}$ depending on variable s_l. (e) Overview of the design method for 3-D read range and a bit sequence.

them, resulting in a lower SNR and reduced reading accuracy, as illustrated in Figure 4.

Therefore, we propose a Root-MUSIC-based signal processing method that achieves accurate estimation of both power and spatial profiles by eigenvalue decomposition. The Root-MUSIC outperforms other signal processing methods including compressive sensing [13] and MUSIC [53], which struggle with estimating either power or spatial profile. Details of the proposed method are described in Section 6.

5 TAG DESIGN

In this section, we present a novel design method for a chipless RFID system based on a CR array. The method addresses the challenge of tag miniaturization while maintaining a wide 3-D read range in terms of distance and angle.

5.1 Minimizing a Corner Reflector Unit

A trihedral CR, consisting of three vertically connected metal plates as shown in Figure 5a, exhibits high RCS at a wide range of angles due to its retroreflective principle. The RCS σ is approximated as follows:

$$\sigma \approx 4\pi A_{\text{eff}}^2/\lambda^2 = 4\pi a^4/3\lambda^2, \tag{10}$$

where a is the side length of a CR, λ is the wavelength of the interrogation frequency, and A_{eff} is the effective area of a CR. However, achieving high RCS is only guaranteed when $a \gg \lambda$. To determine the minimum size required for a CR to achieve high RCS, we conducted electromagnetic simulations with $\lambda = 3.8$ mm corresponding to 79 GHz frequency. Our simulations, as shown in Figure 5b, indicated that the RCS values started to oscillate as a decreased below 4λ. This oscillating zone is called the Rayleigh region [40], in which the incident electromagnetic wave is resonant with the reflector structure. Otherwise, a large RCS is achieved by benefiting from retroreflective properties when $a > 4\lambda$, equivalent to $a >$15.2 mm in the case of 79 GHz mmWave radar interrogation. We concluded that a CR's side length should be more than 15.2 mm for optimal performance.

5.2 Varying RCS Angular Characteristics

As shown in Figure 3b, the RCS of the conventional CR is reduced at θ angles greater than 30°. To overcome this limitation, we propose modifying the shape of the CRs by varying each side length, thereby enabling a larger readable angle. Our investigation into the capability of angular characteristic modification for θ revealed that the side length ratio, defined as $s_l = a_3/a_1 = a_3/a_2$, ($a_1 = a_2$), determines the RCS angle characteristics in both the elevation and the azimuth plane. We defined the operating angle range as the range of angles within which the RCS decreases to less than 5 dB from the maximum RCS. Figure 5c shows that the operating angle range moves to shallower angles as s_l increases from 1 to 3. Additionally, Figure 5d demonstrates that the maximum operational elevation angle θ_{max} and the operational angle range in the azimuth plane ϕ_{width} are trade-offs that depend on s_l. The proposed variable s_l offers a design space for achieving the desired readable angles for various applications. To design tags that can be read from elevation angles up to 60°, the size of a tiny CR was determined as $a_1 = a_2 =$ 23.0 mm and $a_3 =$ 69.1 mm.

5.3 Corner Reflector Array Alignment

This subsection provides the design method for CR alignment, which controls the encoded bit sequence and maximum readable distance. An overview of the design methodology is illustrated in Figure 5e.

5.3.1 Bits Encoding. To enable the accurate reading of bit sequences, an interval of CRs aligned along the ground range d_x is essential (Figure 2). The interval d_x must account for both radar distance resolution and look angle to ensure sufficient readability at any angle combination (θ_u, ϕ_u), where

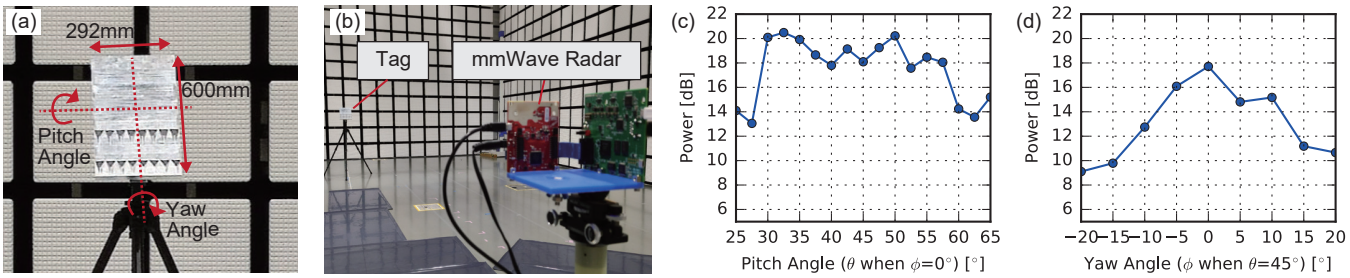

Figure 6: (a, b) View of the measurement setup from 10 m away in a large anechoic chamber. The fabricated tag is encoded with 8-bit and $n_y = 8$. (c, d) Measured reflected power of tags at various incident angles θ (c) and ϕ (d).

$d_x \geq R_{res}$ is necessary. This leads to the requirement for $d_x \geq R_{res}/(\sin\theta_u \cos\phi_u)$, and the minimum look angle θ_{min} can be designed as

$$\theta_{min} = \arcsin(\frac{R_{res}}{d_x}), \tag{11}$$

where R_{res} is the radar distance resolution. To achieve $\theta_{min} = 30°$, we set $d_x = 75$ mm, where $R_{res} = 37.5$ mm.

5.3.2 Distance Expansion. Alignment, along with cross-range direction (*i.e.*, y-axis), increases the total RCS and reading distance. Yet, those CRs can be recognized as one-bit reflectors from a MIMO radar with a low angle resolution of 14°, as described in Subsection 3.2. The RCS of the CR-cross range array σ_{array} can be approximated from the number of alignment n_y as $\sigma_{array}(\theta_u, \phi_u) = n_y^2 \sigma_{cr}(\theta_u, \phi_u)$, where σ_{cr} represents the RCS of a CR unit. Then, from Eq. (2), the maximum readable distance R_{max} is expressed as follows:

$$R_{max} = n_y^{\frac{1}{2}} \left[\frac{P_t \lambda^2 G(\theta_u + \theta_e, \phi_u + \phi_e)^2 \sigma_{cr}(\theta_u, \phi_u)}{(4\pi)^3 S_{min}} \right]^{1/4}. \tag{12}$$

Through the investigation, we can relate the distance, elevation angles, and azimuth angles to the tag design parameters, as shown in Figure 5e.

We fabricated a CR array encoding 8 bits with $n_y = 8$. The measurements were conducted in a large anechoic chamber at a distance of 10 m, as shown in Figure 6a and b. The results with varying incident angles in terms of θ and ϕ are shown in Figure 6c and d. The results validated the wide angular characteristics of the tag in both pitch and yaw angles.

6 SIGNAL PROCESSING

This section describes a signal processing method of tag detection from raw radar signals. Root-MUSIC is adopted for obtaining the frequency components (*i.e.*, range components in localization) as roots in the IF signals. By combination with clustering algorithm DBSCAN, an automatic tag detection pipeline is developed.

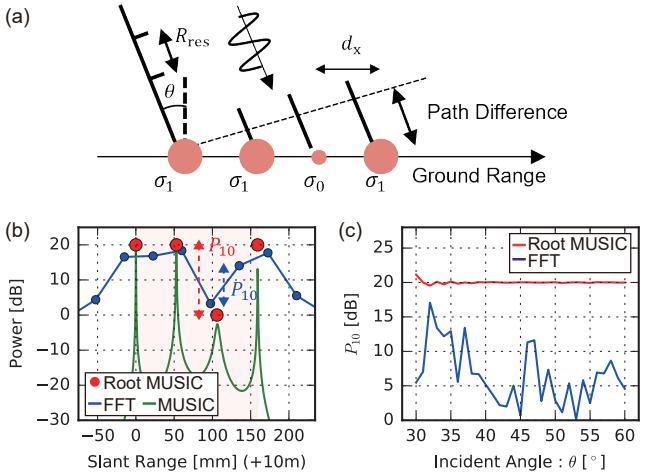

Figure 7: (a) Simulation model of reflector allocation and radar. (b) Obtained range power profiles with FFT, MUSIC, and Root-MUSIC. (c) SNR (P_{10}: power ratio between bits "0" and "1") with the varying look angle.

6.1 Root-MUSIC with Look Angle Tolerance

Root-MUSIC extracts the signal's frequency components by performing an eigenspace decomposition of the signal's autocorrelation matrix R. Once the size M of the matrix R is determined, an M degree polynomial $Q(z)$ is obtained through the eigenvalue decomposition of R, as follows:

$$Q(z) = \sum_{k=1}^{M} p^H(z^{-1}) v_k v_k^H p(z) = 0, \tag{13}$$

where v_k is the k-th eigenvector of R and $p(z)$ is the mode vector expressed as $p(z) = [1, z, z^2, ..., z^{M-1}]^t$. The roots $z_m (1 \leq m \leq M)$ are obtained by solving $Q(z) = 0$. z_m are a complex value, expressed as:

$$z_m = e^{h_m \Delta t + j 2\pi f_m \Delta t}, \tag{14}$$

where h_m is the amplitude change rate and f_m is the frequency. The complex amplitude corresponding to each root

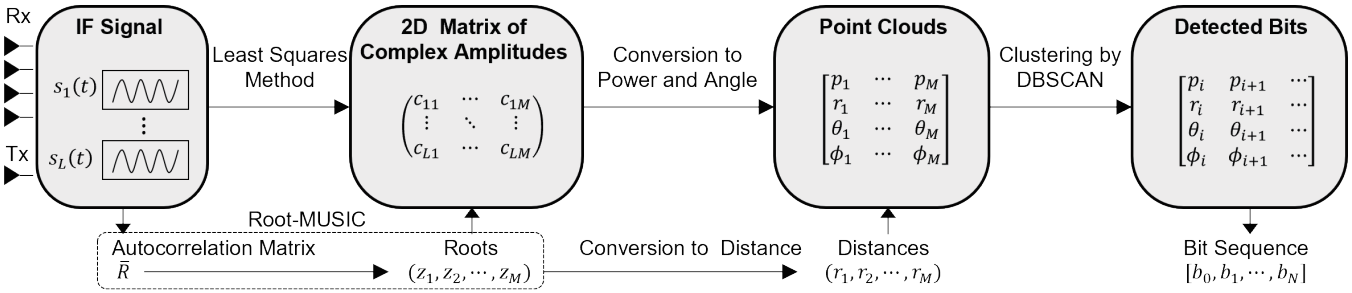

Figure 8: Proposed signal process pipeline of computing roots, power estimation, 3-D localization, and tag detection from a multidimensional raw radar signal.

z_{m} is obtained using the least squares method with $s(t)$. Next, the obtained frequency and complex amplitude can be converted to distances as $r_{\mathrm{m}} = f_{\mathrm{m}} \cdot cT/2B$ and signal power as $P_{\mathrm{m}} = |c_{\mathrm{m}}|^2$, respectively. The analysis results obtained as roots are less susceptible to slight changes in frequency components, enabling a robust readout even in the presence of variations in the look angle.

To validate the look angle tolerance, a simulation was conducted comparing the performance of Root-MUSIC with FFT and MUSIC. The simulation model of slant range reading is shown in Figure 7a, where different RCS reflectors on a tag are aligned with equal intervals so that the encoded bit sequence becomes "1101." RCSs of scatterers corresponding to bits "1" and "0" are defined as σ_1 and σ_0, and their ratio σ_1/σ_0 is equal to 20 dB. The distance r_{u} is set as 10 m, and the reflector interval d_{x} is fixed as $2R_{\mathrm{res}}$. Figure 7b shows the results when $\theta_{\mathrm{u}} = 45°$, demonstrating that Root-MUSIC accurately decoded the embedded sequence, whereas FFT failed to correctly capture the bit sequence. Although MUSIC also achieved high accuracy in range estimation, it only outputs a continuous function.

To quantify the look angle tolerance, the power ratio of bits "0" to "1", P_{10} was calculated with FFT and Root-MUSIC through look angles from 30° to 60°. P_{10} computed by FFT degraded irregularly at some look angles, but the Root-MUSIC method maintained high values at every angle (Figure 7c).

6.2 Calculating Representative Roots for 3-D Localization

Using Root-MUSIC, we develop the signal processing pipeline from IF signals received in multiple antennas to automatic tag detection and readout of the bit sequence. The entire process pipeline is shown in Figure 8. To achieve 3-D localization, the representative roots are calculated by averaging the autocorrelation matrix as follows:

$$\overline{R} = \frac{1}{L}\sum_{l=1}^{L} R^{(l)}, \tag{15}$$

where $R^{(l)}$ is the autocorrelation matrix of IF signal $s_{\mathrm{l}}(t)$ recieved at the l-th antenna ($1 \le l \le L$). By using $\overline{R}$, the common roots among antennas are obtained. The Root-MUSIC and least squares methods are then applied to obtain the pair of roots and complex amplitudes $(z_{\mathrm{m}}, c_{\mathrm{lm}})$. The phase rotation of complex amplitudes c_{lm} depends on the angle of arrival of the reflector. Thus, calculating the velocity of phase rotation in c_{lm}, $(1 \le l \le L)$ gives the estimated angles θ_{m} and ϕ_{m} [21]. Thus, we can obtain point clouds with power, distance, and angle information.

6.3 Automatic Tag Detection

The calculated roots provide accurate spatial and power profiles. Since the detected roots corresponding to our developed tag have power and spatial proximity, clustering based on distances in 4-D space consisting of the power (1-D) and position (3-D) offers the ability to distinguish the tag from other highly reflective objects. Thus, we use DBSCAN [15], a classical density-based clustering algorithm, to automatically detect the tag. The robustness of tag detection in noisy environments is validated in Section 7. The method can be processed offline for autonomous control.

7 EVALUATION

To evaluate MilliSign, we conducted experiments using a prototype UAV equipped with a mmWave radar and an aluminum tag. In this section, we present our experimental methodology and results, highlighting the system's practicality with respect to 3-D read range, readout accuracy, robustness to poor visibility conditions, UAV motion, multipath interference, and the effect of background surfaces.

7.1 Experimental Setup

We developed a mmWave radar-mounted UAV equipped with positioning and posture sensors such as IMU [12], LiDAR altimeter [45], GPS [51], and a tablet Windows PC, which calculated the relative position of the UAV to the tag.

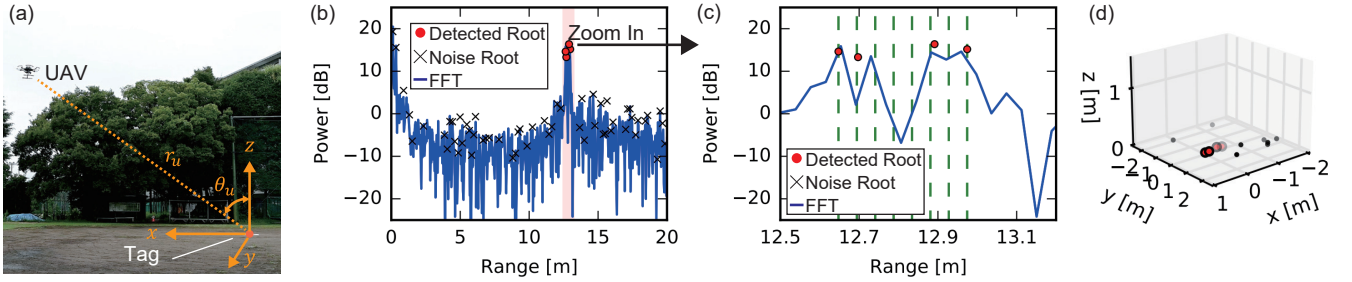

Figure 9: (a) Experimental view of the UAV measuring with the coordinates. (b) Analysis results of the range power profile of the proposed Root-MUSIC-based method (red dots and black crosses) and the conventional FFT-based method (blue line). The marker of the roots is automatically determined by DBSCAN clustering. (c) Results zoomed in on the area where the tag was placed. (d) 3-D localization results of the detected roots (red and black circles represent the tag and noise, respectively).

The experiments used a TI radar [23] with carrier frequency $f_c = 79$ GHz, chirp bandwidth $B = 4.0$ GHz, and chirp duration $T_c = 110$ μs. The polarization of the radar was set to vertical. Each radar measurement was conducted with the consecutive chirp of $N = 32$ with an interval of 200 μs.

The CR array tags shown in Figure 6 were used, and two types of tag placement were tested using horizontal and vertical placeholders made using shaped styrofoam. The UAV followed a pre-programmed flight path with a series of waypoints. The hyperparameter M in Root-MUSIC was set to 100, corresponding to the number of detected roots.

7.2 Readout Demonstration

7.2.1 Single Tag Readout. We conducted radar measurements at a UAV position of $(r_u, \theta_u, \phi_u) = (12.6\text{m}, 45°, 0°)$ in the polar coordinate system shown in Figure 9a with a horizontally installed tag representing a bit pattern of "11000101." The results from conventional FFT and the proposed Root-MUSIC-based method are presented in Figure 9b and c, which display the range power profile at the UAV position. The Root-MUSIC-based method detected four reflectors encoded as bit 1, while range FFT failed to decode the bit sequence. Moreover, by clustering with DBSCAN, roots corresponding to the tag could be detected because they had the same level of reflected power and spatial proximity. The estimated distances to the roots in the slant range were precise, as indicated by the good agreement with the green dotted lines equally divided by the bit length 8 between the first and last range values in Figure 9c. Figure 9d shows the 3-D localizing results. The distance estimation error was 3.5 mm, while the average angle estimation error was 0.55° in azimuth and 0.97° in elevation. The azimuth angle accuracy was higher than that for the elevation since the radar has eight virtual antenna elements in the azimuth and two in the elevation plane. The results validate the effectiveness of the Root-MUSIC-based method in accurately detecting, decoding, and localizing tags.

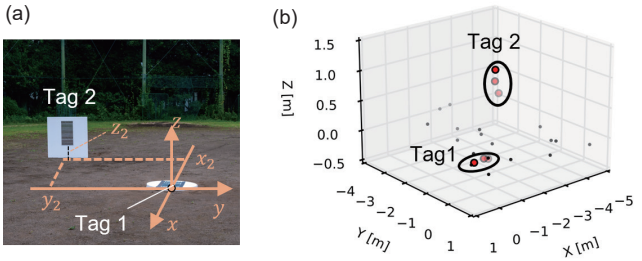

Figure 10: (a) A view of signs placed horizontally and vertically. (b) 3-D localization results of the detected roots in red and noise in black.

7.2.2 Simultaneous Readout of Multiple Tags. The simultaneous readout of multiple tags was validated by conducting experiments using tags placed in different positions and encoded by different bit sequences. The first tag, with a bit sequence of "10000101," was placed horizontally at the origin, while the second tag was installed vertically at $(x_2, y_2, z_2) = (-4, -3, 0.6)$ with a bit sequence of "10001001." Vertically installed tags could also be read since their large RCS maintained with a look angle θ_u of 30° to 60°, as demonstrated in Figure 6c. The measurement was conducted at a UAV position of $(r_u, \theta_u, \phi_u) = (12.6\text{m}, 45°, 0°)$. The results, shown in Figure 10b, reveal that the system accurately interpreted the bit sequences and precisely estimated the tags' locations without tag-to-tag interference.

7.3 Readout Performance Evaluation

7.3.1 Evaluation Metrics. In the experiments, we used the SNR of the coding peaks and the detection rate as evaluation metrics. Higher SNRs indicate more prominent coding

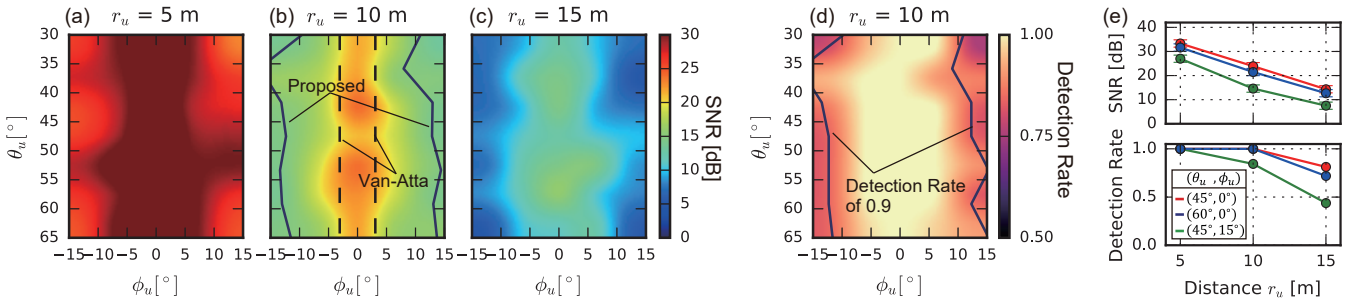

Figure 11: (a, b, c) SNR distribution with different angles θ_u, ϕ_u at specified distance r_u in the polar coordinate system shown in Figure 9. In (b), the contour lines are drawn to show the boundary of the value of 15.8 dB in SNR. The performance of the Van Atta array antenna as the baseline is shown as dotted lines. (d) Detection rates at varying azimuth and elevation angles at a distance of 10 m, with boundary lines indicating a value of 0.9. (e) SNR and detection rates at varying distances with three angles $(\theta_u, \phi_u) = (45°, 0°), (60°, 0°)$, and $(45°, 15°)$.

peaks that are easier to decode. We calculated the SNR as $(\mu_1 - \mu_0)^2/\sigma^2$, where μ_i is the average amplitude of bit "i" and σ is the standard deviation of the coding peak amplitudes. As our method may fail to detect bit "0" due to its lower reflected power than the background noise, we obtained μ_0 by averaging the power corresponding to the noise roots, as shown in Figure 9b. The SNR can be mapped to the BER by using the on-off keying model, with BER $= \frac{1}{2}\mathrm{erfc}(\sqrt{\mathrm{SNR}/8})$[44]. We used the bit pattern "101" in subsequent experiments for obtaining SNRs. The detection rate was computed by determining the number of successful detections within a series of $N = 32$ consecutive measurements. The success of each detection was gauged by validating the following requirements: the extraction of roots associated with tags via clustering, the resulting bit pattern, and the estimated position.

7.3.2 3-D Read Range. Experiments were conducted to evaluate the 3-D read range in terms of distance, azimuth angle, and elevation angle. Waypoints were set to scan the tag for three distances, 5 m, 10 m, and 15 m, with θ_u ranging from 30° to 65° and ϕ_u ranging from −15° to 15°. The obtained SNRs are shown in Figure 11a, b, and c with the different distances r_u. In Figure 11b, continuous lines are drawn to show the boundary of the value of 15.8 dB in SNR, and the dotted lines are drawn to show the same values of the boundary if the Van Atta arrays, which have a narrow beam width of 1.27°, are used instead of the CR array-based tag. We achieved a total area 7.8 times larger than the wide 3-D readout area of the Van Atta array-based method.

Detection rates at 10 m with varying angles in azimuth and elevation were calculated (Figure 11d). The result showed that detection rates of 0.9 or higher were achieved with an angle width of 30° in elevation and 20° in azimuth. A comparison of Figure 11b and d show that SNRs and detection

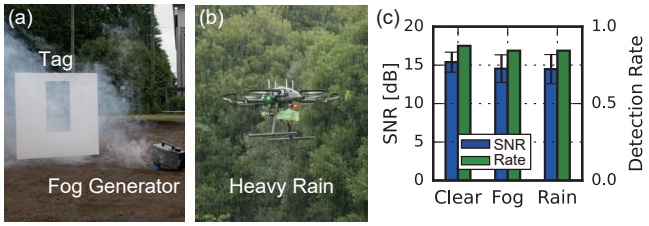

Figure 12: (a) Emulated foggy environment with a fog generator. (b) UAV flight measuring under heavy rain at a precipitation rate of approximately 5 mm/h. (c) SNRs and detection rates under poor visibility conditions.

rates were roughly proportional except in the angles where the detection rates remain high at 1.0. Figure 11e shows the effect of distance change on detection performance with three angles. SNRs and detection rates were decreased with increasing distance. The detection rate starts to decrease when the SNR is less than 17.5 dB. At 15 m, the detection rate is below 0.9 for all angles, indicating that the distance has a significant impact on performance. The reduction in SNRs and detection rates at far distances can be compensated by increasing the number of CR alignments n_y, as formulated in Eq. (12).

These findings show that the system performs well enough to guide UAVs to approach the tag, like a precision approach path indicator, realizing a range of applications such as landing on ships and retrieving luggage.

7.3.3 Robustness to Poor Visibility. mmWave radar exhibits robustness to inclement weather such as fog and rain, unlike optical rays. The attenuation at 79 GHz due to heavy fog (water droplet concentration 1 mg/m^3) is about 2 dB per 100 m [4], while that due to torrential rain (precipitation 100 mm/h) is only slightly higher (3.2 dB per 100 m) [55]. We

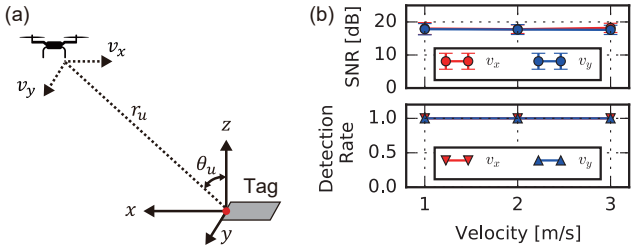

Figure 13: (a) Experimental configuration for robustness to the UAV's velocity. (b) Measured SNR and detection rates indicate that no deterioration occurs with different velocities.

validated the ability of our system to function under poor visibility conditions by conducting outdoor experiments when a fog generator [36] was running and it was raining at a precipitation rate of approximately 5 mm/h. The tag was placed vertically on the styrofoam wall (Figure 12a). Measurements were taken at an angle of $(\theta_u, \phi_u) = (45°, 0°)$ and distance $r_u = 15$ m, and the results were compared with those obtained under clear conditions. Figure 12 shows that the measured SNR and detection rates remained stable, indicating all-weather guidance capability.

7.3.4 Readout Performance while Moving. We investigated the ability to perform readouts while moving, which can reduce operational costs in various scenarios, including retrieving luggage. When interrogating radar signals travel between the tag and the UAV, slight changes in the UAV's position may affect readout performance [10]. However, our system is robust to motion because the UAV's speed is at most 10 m/s, which causes only 1 μm of distance deviation during the electromagnetic wave's round trip of several tens of meters. To validate this, we conducted experiments with different UAV speeds and directions of movement v_x, v_y. The measurements were conducted at the fixed point $(r_u, \theta_u, \phi_u) = (12\text{ m}, 45°, 0°)$ with the tag installed vertically, as shown in Figure 13a. Figure 13b presents the measured SNR and detection rates, which demonstrated consistently high values across all speeds and directions, indicating the negligible impact of UAV velocity on readout performance.

7.3.5 Robustness to Multipath Effect. MilliSign is highly robust to interference from surrounding obstacles and the multipath effect. This is due to the tag's low reflectivity for incident waves of unintended angles, which prevents interference from large obstacles in a multipath-rich environment. We conducted experiments in two environments: (i) with a van and a wall placed around the tag and (ii) near stairs, which seem to be among the most difficult situations in urban spaces, since they cause significantly large reflections.

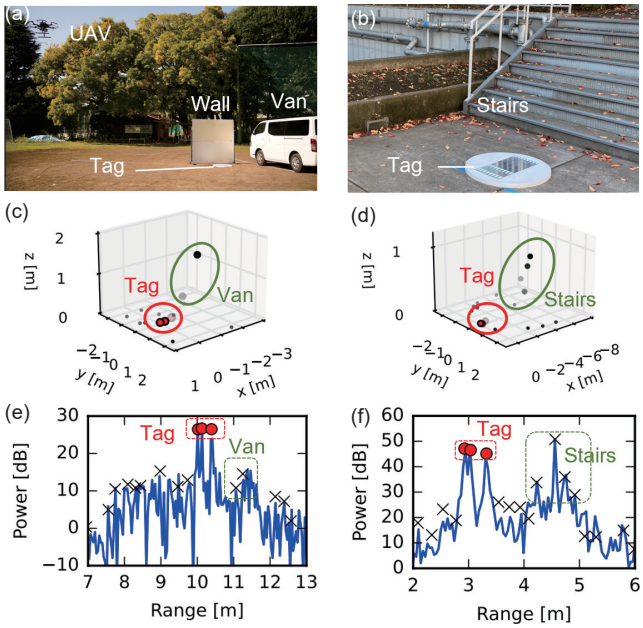

Figure 14: (a, b) Experimental view of multipath-rich environments. (c, d) 3-D localization results with detected roots. (e, f) Results of range power profiles with clustered roots.

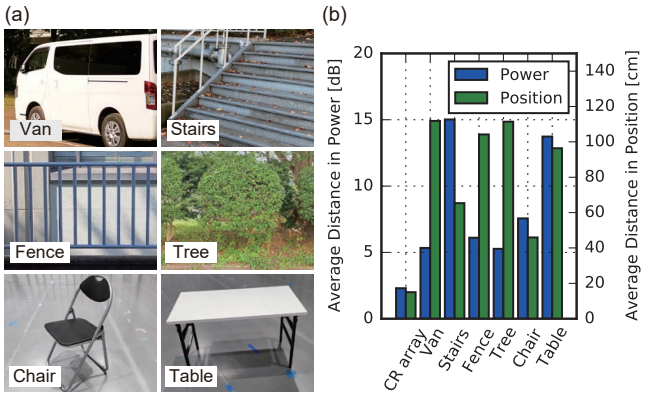

Figure 15: (a) Appearances of evaluated objects. (b) Measured results of average distance in power and position. Our tag (CR array) exhibited short distances in both power and spatial dimensions, while other objects had large distances in either power or spatial dimension.

The experimental view was as shown in Figure 14a and b. In environment (i), a 5 m sized van was parked 1.5 m behind the tag and a 2 m square metal wall was placed 1 m from the tag, which represented a bit pattern of "10100001." Figure 14c and e show the localized roots and range power profiles, respectively. Although large reflections from the van's surface were observed, our tag had a 10.2 times larger reflection than

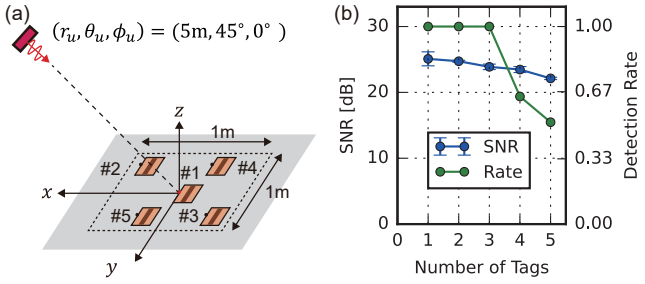

Figure 16: (a) Multiple tags were placed on the ground. (b) Calculated SNRs and detection rates. The detection rate decreased when there were 4 or 5 tags, while the SNR remained high, surpassing 20 dB for 1 to 5 tags.

the van, which indicates the tag is easy to detect even in the presence of surrounding obstacles.

In environment (ii), the tag was placed 1 m in front of the stairs. The measurement was conducted with the radar fixed by a tripod since UAVs were not allowed to fly at that location for safety reasons. Although the results in Figure 14f show that the stairs had strong reflection comparable to our tag, a large variation appeared in received power from the stairs. In contrast, the roots corresponding to our tag had both ordered spatial patterns and the same extent of reflected power, which facilitated automatic tag detection by DBSCAN.

To further investigate the robustness of the tag detection in terms of its small deviation of detected roots in both power and position, we evaluated various reflective objects including vans, stairs, fences, trees, chairs, and tables, which are shown in Figure 15a. The measurements were conducted at a distance of 5 m from the objects. Figure 15b shows the average distances of obtained point clouds ("roots") in terms of power and position. The experiments revealed that only our developed tag demonstrates the short distances in both spatial (less than 20 cm) and power (less than 3 dB) dimensions, while other objects had large distances in either power or spatial dimensions. The distinctive properties in spatial power dimensions facilitate automatic detection with the robustness of the surrounding objects and the multipath-rich environment, which are common in urban spaces.

7.3.6 Mutliple Tag Dection. The detection performance, in scenarios involving multiple tags, was assessed. This evaluation was conducted when up to five tags were simultaneously placed within a 1 m square area as shown in Figure 16a. The measurements were carried out in the anechoic chamber, with the radar position fixed at $(r_\text{u}, \theta_\text{u}, \phi_\text{u}) = (5\text{m}, 45°, 0°)$. All tags possessed a bit pattern of "101." The coordinates of tags (x_i, y_i), $\{1 \le i \le 5\}$ were set as follows: $(x_1, y_1) = (0, 0)$, $(x_2, y_2) = (1.0, -0.85)$, $(x_3, y_3) = (-0.75, 0.85)$, $(x_4, y_4) = (0.5, 0.85)$, and $(x_5, y_5) = (-0.5, -0.75)$. The measurements were conducted by incrementally increasing the number of tags from 1 to 5.

The results, shown in Figure 16(b), indicated a high SNR exceeding 20 dB for 1 to 5 tags. However, the detection rate dropped when there were four or five tags. A high SNR with multiple tags led to a lower detection rate due to the dense point clouds with close power levels, requiring more accurate spatial estimation. It is expected that increasing spatial resolution, using a radar with a wider bandwidth or more MIMO antennas, could improve the detection rate in multi-tag scenarios.

7.3.7 Performance with Various Background Surfaces. We explored the impact of surface type on MilliSign's performance by measuring the strength of backscatter for four surface types, sand, grass, water, and metal, as shown in Figure 17a, b, c, and d. Using an antenna pole, the mmWave radar was positioned at a height of 5 m with a slanted angle of 45°, and two types of tag were placed horizontally 5 m from the pole. The results (Figure 17e) demonstrate that the CR array with $n_\text{y} = 8$ had a significantly stronger reflection, by 20 dB, than sand and grass surfaces, whereas water and metal surfaces exhibited lower levels of backscatter. These findings suggest that the smoothness of the surface impacted the backscattered intensity and the background noise level. We concluded that by minimizing the tag size through decreasing n_y, the smaller tag could be deployed on water or metal surfaces.

7.3.8 Latency. The proposed signal processing pipeline exhibited low latency of 152 ms. Despite the high computational demands of multi-dimensional MUSIC techniques [6, 16, 53], our Root-MUSIC-based signal processing, which utilizes representative roots, had a computational cost similar to that of one-dimensional MUSIC. The bottleneck in our processing pipeline was the calculation of the least squares method for obtaining a 3-D complex amplitude matrix. When the sample size of the IF signal is denoted as N_d, computational complexity was $O(M^2 \cdot N_\text{d}) = 2.6 \cdot 10^6$ for $M = 100$ and $N_\text{d} = 256$ in our experiments. The low computation cost paves the way for real-time applications of MilliSign technology.

8 DISCUSSION

This section discusses the applications and practicalities of Millisign. The current limitations are also described.

8.1 Read Range

Readout Distance: The experimental results demonstrated a detection rate of 1.0 at 10 m. This readout distance is longer than conventional RFID [31] and RoS [33]. Moreover, tag design can adapt according to specific requirements, as Eq. (12) confirms the trade-off between maximum readable distance and tag size.

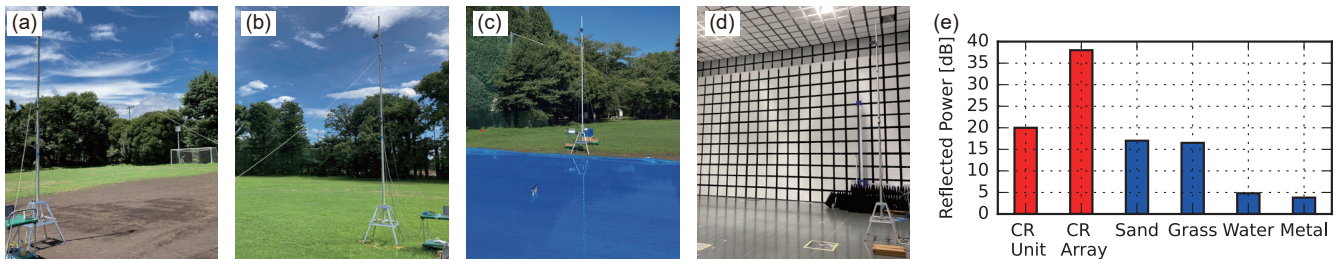

Figure 17: Experiments were conducted to measure the intensity of backscattering reflection from four types of surfaces: (a) sand, (b) grass, (c) water, and (d) metal. (e) Backscatter intensity was measured compared with the fabricated tag: a CR unit with $n_y = 1$ and a CR array with $n_y = 8$ as references.

Read Angle and Tag Orientation: The proposed detection algorithm offers robustness to misalignment in tag orientation. The experiments in Figure 11 demonstrated a wide read angle of more than 30 ° in elevation and 20 ° azimuth. The angle range could be broadened by optimizing CR arrangement, which may result in a decrease in readout distance. Regarding the limitation on the readout from the direction perpendicular to the tag, combining multiple readouts and applying SAR-based techniques can mitigate this limitation. For instance, using single readouts when the tag is far away and switching to SAR-based readouts in the proximity of the tag can take advantage of both approaches. Furthermore, bit order flipping can be prevented since the tag does not reflect radar signals coming from outside the intended read range.

8.2 Applicability

Impact of mmWave Radar as Payloads: A mmWave radar sensor is small, lightweight, and low-powered, which naturally leads to it being mounted on a UAV to achieve high autonomous capability. The TI mmWave radar is about 5 cm square, weighs about 30 g, and consumes about 1.5 W. Considering that industrial UAVs can carry a payload of more than several kilograms and consume more than 100 W, the mounting of mmWave radars has little impact on UAVs.

Weight of the Tag: The weight of the tag is an essential factor, considering that UAVs transport packages with tags attached. Although the used CR unit fabricated through CNC machining is heavy at 42 g, a lightweight design is achievable using thin aluminum foil, given the skin depth at the operational frequency is 0.4 μm.

Implementation Cost: The cost of the radar ICs is around US$ 30. Since mmWave radar sensors have already been integrated into commercial IoT devices, software development and integration to UAVs are likely to be straightforward. The prototype tags were manufactured using CNC aluminum machining, which cost around US$ 100. However, the cost of the tags can be reduced by producing metal molds. Overall, the cost of deploying MilliSign, including developing the mmWave radar system and tag fabrication, should be reasonable. This is particularly true considering that industrial-grade UAVs typically cost around US$ 500.

Debris Entry: The tags need to be protected from dust, sand, mud, and water (rain), which can enter and deteriorate the backscattering RCS of the tag when installed on the ground. The use of a radome, known for its interference-free protection of radar antennas [20], to cover the tag for the mmWave band would solve this problem.

Encoding Capacity: 8-bit encoding was realized, which can convey several hundreds of different messages to the UAVs. In logistics, where the number of cargo types is limited to several tens, the system can be used to convey cargo information on both type and weight. MilliSign can also serve as a concretized landing port, such as a precision approach path indicator (PAPI), and offer an additional message such as the type of vehicle on which the tag is installed. Although the current 8-bit information is useful, advanced modulation schemes such as amplitude modulation by changing the RCS of each bit can improve the information density, making it even more practical for a broader range of applications.

9 CONCLUSION

In this paper, we developed MilliSign, an all-weather UAV guidance system with batteryless tags. The system incorporates two newly developed techniques: CR array-based spatial chipless RFID and the Root-MUSIC-based readout method. We validated its practicality in real-world environments through extensive experiments. We believe that this study will provide a foundation for future research and development of all-weather tolerant UAV flights.

REFERENCES

[1] Wilbert G. Aguilar, Guillermo A Rodríguez, Leandro Álvarez, Sebastián Sandoval, Fernando Quisaguano, and Alex Limaico. 2017. Visual SLAM with a RGB-D camera on a quadrotor UAV using on-board processing. In *Advances in Computational Intelligence: 14th International Work-Conference on Artificial Neural Networks, IWANN 2017, Cadiz, Spain,*

June 14-16, 2017, Proceedings, Part II 14. Springer, 596–606.

[2] Larry M. Arjomandi, Grishma Khadka, and Nemai C. Karmakar. 2021. mm-Wave chipless RFID decoding: introducing image-based deep learning Techniques. *IEEE Transactions on Antennas and Propagation* (May 2021).

[3] Ashkan Azarfar, Nicolas Barbot, and Etienne Perret. 2022. Chipless RFID based on micro-doppler effect. *IEEE Transactions on Microwave Theory and Techniques* 70, 1 (Jan. 2022), 766–778.

[4] Nezah Balal, Gad A. Pinhasi, and Yosef Pinhasi. 2016. Atmospheric and fog effects on ultra-wide band radar operating at extremely high frequencies. *Sensors* 16, 5 (2016), 751.

[5] Santanu Kumar Behera and Nemai Chandra Karmakar. 2021. Chipless RFID printing technologies: A state of the art. *IEEE Microwave Magazine* 22, 6 (Jun. 2021), 64–81.

[6] Francesco Belfiori, Wim van Rossum, and Peter Hoogeboom. 2012. Application of 2D MUSIC algorithm to range-azimuth FMCW radar data. In *2012 9th European Radar Conference*. IEEE, 242–245.

[7] Michele Borgese, Simone Genovesi, Giuliano Manara, and Filippo Costa. 2021. Radar cross section of chipless RFID tags and BER performance. *IEEE Transactions on Antennas and Propagation* 69, 5 (2021), 2877–2886.

[8] Katelyn R. Brinker and Reza Zoughi. 2020. Corner reflector based misalignment-tolerant chipless RFID tag design methodology. *IEEE Journal of Radio Frequency Identification* 5, 1 (2020), 94–105.

[9] Shuhui Bu, Yong Zhao, Gang Wan, and Zhenbao Liu. 2016. Map2DFusion: Real-time incremental UAV image mosaicing based on monocular SLAM. In *2016 IEEE/RSJ International Conference on Intelligent Robots and Systems (IROS)*. IEEE, 4564–4571.

[10] Michael Caris, Stephan Stanko, Mateusz Malanowski, Piotr Samczyński, Krzysztof Kulpa, Arnulf Leuther, and Axel Tessmann. 2014. mm-Wave SAR demonstrator as a test bed for advanced solutions in microwave imaging. *IEEE Aerospace and Electronic Systems Magazine* 29, 7 (2014), 8–15.

[11] Baicheng Chen, Huining Li, Zhengxiong Li, Xingyu Chen, Chenhan Xu, and Wenyao Xu. 2020. ThermoWave: A new paradigm of wireless passive temperature monitoring via mmWave sensing. In *Proceedings of the 26th Annual International Conference on Mobile Computing and Networking (MobiCom '20)*. 1–14.

[12] SYD Dynamics. 2022. TransducerM TM200 - SYD Dynamics. Retrieved Aug. 9, 2022 from https://www.syd-dynamics.com/transducerm_tm200/.

[13] Joachim H.G. Ender. 2010. On compressive sensing applied to radar. *Signal Processing* 90, 5 (2010), 1402–1414.

[14] Milan Erdelj and Enrico Natalizio. 2016. UAV-assisted disaster management: Applications and open issues. In *2016 International Conference on Computing, Networking and Communications (ICNC)*. IEEE, 1–5.

[15] Martin Ester, Hans-Peter Kriegel, Jörg Sander, and Xiaowei Xu. 1996. A density-based algorithm for discovering clusters in large spatial databases with noise. In *kdd*, Vol. 96. 226–231.

[16] Andrey A. Geltser and Evgeny A. Monastyrev. 2015. MUSIC-based algorithm for range-azimuth FMCW radar data processing without estimating number of targets. *2015 IEEE 15th Mediterranean Microwave Symposium (MMS)* (2015), 1–4.

[17] Markus Gerke and Heinz-Jürgen Przybilla. 2016. Accuracy analysis of photogrammetric UAV image blocks: Influence of onboard RTK-GNSS and cross flight patterns. *Photogrammetrie, Fernerkundung, Geoinformation (PFG)* 1 (2016), 17–30.

[18] G. Greco, C. Lucianaz, S. Bertoldo, and M. Allegretti. 2015. Localization of RFID tags for environmental monitoring using UAV. In *2015 IEEE 1st International Forum on Research and Technologies for Society and Industry Leveraging a better tomorrow (RTSI)*. IEEE, 480–483.

[19] Cristian Herrojo, Ferran Paredes, Javier Mata-Contreras, and Ferran Martín. 2019. Chipless-RFID: A review and recent developments. *Sensors* 19, 15 (2019), 3385.

[20] Maruf Md Sajjad Hossain, Syed An Nazmus Saqueb, Alebel H Arage, John Cabigao, Carlos Velasquez, Kubilay Sertel, and Niru K Nahar. 2021. Wideband radomes for millimeter-wave automotive radars. *IEEE Transactions on Antennas and Propagation* 70, 2 (2021), 1178–1186.

[21] Tatsuya Iizuka, Yohei Toriumi, Fumihiko Ishiyama, and Jun Kato. 2020. Root-MUSIC based power estimation method with super-resolution FMCW radar. In *2020 IEEE/MTT-S International Microwave Symposium (IMS)*. IEEE, 1027–1030.

[22] Jun Inoue and Kazutoshi Sato. 2022. Toward sustainable meteorological profiling in polar regions: Case studies using an inexpensive UAS on measuring lower boundary layers with quality of radiosondes. *Environmental Research* 205 (Apr. 2022), 112468. https://doi.org/10.1016/j.envres.2021.112468

[23] Texas Instruments. 2019. TI IWR1443 single-chip 76-GHz to 81-GHz mmWavesensor evaluation module. Retrieved Mar. 16, 2023 from https://www.ti.com/tool/IWR1443BOOST.

[24] Vikram Iyer, Maruchi Kim, Shirley Xue, Anran Wang, and Shyamnath Gollakota. 2020. Airdropping sensor networks from drones and insects. In *Proceedings of the 26th Annual International Conference on Mobile Computing and Networking (MobiCom '20)*. 1–14.

[25] Chengkun Jiang, Junchen Guo, Yuan He, Meng Jin, Shuai Li, and Yunhao Liu. 2020. mmVib: Micrometer-level vibration measurement with mmwave radar. In *Proceedings of the 26th Annual International Conference on Mobile Computing and Networking (MobiCom '20)*. 1–13.

[26] Alejandro Jiménez-Sáez, Martin Schüßler, Mohammed El-Absi, Ali Alhaj Abbas, Klaus Solbach, Thomas Kaiser, and Rolf Jakoby. 2020. Frequency selective surface coded retroreflectors for chipless indoor localization tag landmarks. *IEEE Antennas and Wireless Propagation Letters* 19, 5 (2020), 726–730.

[27] Sophie Jordan, Julian Moore, Sierra Hovet, John Box, Jason Perry, Kevin Kirsche, Dexter Lewis, and Zion Tsz Ho Tse. 2018. State-of-the-art technologies for UAV inspections. *IET Radar, Sonar & Navigation* 12, 2 (2018), 151–164.

[28] Zhengxiong Li, Baicheng Chen, Zhuolin Yang, Huining Li, Chenhan Xu, Xingyu Chen, Kun Wang, and Wenyao Xu. 2019. FerroTag: A paper-based mmWave-scannable tagging infrastructure. *SenSys 2019 - Proceedings of the 17th Conference on Embedded Networked Sensor Systems*, 324–337. https://dl.acm.org/doi/10.1145/3356250.3360019

[29] Zhilin Lyu, Weitao Ding, Xiujun Sun, Hongqiang Sang, Ying Zhou, Peiyuan Yu, and Lijun Zheng. 2021. Dynamic landing control of a quadrotor on the wave glider. *Journal of Marine Science and Engineering* 9, 10 (2021).

[30] Gary Melvin, Yanchao Li, Larry Mayer, and Allan Clay. 2002. Commercial fishing vessels, automatic acoustic logging systems and 3D data visualization. *ICES Journal of Marine Science* 59, 1 (2002), 179–189.

[31] Hetal P. Mistry and Nital H. Mistry. 2015. RSSI based localization scheme in wireless sensor networks: A survey. In *5th International Conference on Advanced Computing & Communication Technologies*. IEEE, 647–652.

[32] Dong Huu Nguyen, Mohammad Zomorrodi, and Nemai Chandra Karmakar. 2019. Spatial-based chipless RFID system. *IEEE Journal of Radio Frequency Identification* 3, 1 (2019), 46–55.

[33] John Nolan, Kun Qian, and Xinyu Zhang. 2021. RoS: passive smart surface for roadside-to-vehicle communication. In *Proceedings of the ACM SIGCOMM 2021 Conference*. 165–178.

[34] Code of Federal Regulations. 2023. eCFR :: 14 CFR Part 107 – Small unmanned aircraft systems (FAR part 107). Retrieved Mar. 16, 2023 from https://www.ecfr.gov/current/title-14/chapter-I/subchapter-F/part-107#107.29.

[35] Umberto Papa and Giuseppe Del Core. 2015. Design of sonar sensor model for safe landing of an UAV. In *2015 IEEE Metrology for Aerospace (MetroAeroSpace)*. IEEE, 346–350.

[36] Parrot. 2021. Z-800II mobility and portability fog machine - Antari lighting and effects . Retrieved Aug. 8, 2022 from https://antari.com/products/z-800ii/.

[37] Kun Qian, Zhaoyuan He, and Xinyu Zhang. 2020. 3D point cloud generation with millimeter-wave radar. *Proceedings of the ACM on Interactive, Mobile, Wearable and Ubiquitous Technologies* 4, 4 (Dec. 2020), 1–23.

[38] Kun Qian, Lulu Yao, Xinyu Zhang, and Tse Nga Ng. 2022. MilliMirror: 3D printed reflecting surface for millimeter-wave coverage expansion. In *Proceedings of the 28th Annual International Conference on Mobile Computing and Networking (MobiCom '22)*. 15–28.

[39] Taweesak Sanpechuda and La-or Kovavisaruch. 2008. A review of RFID localization: Applications and techniques. In *2008 5th International Conference on Electrical Engineering/Electronics, Computer, Telecommunications and Information Technology*, Vol. 2. IEEE, 769–772.

[40] Merrill I. Skolnik. 2008. *Radar Handbook*. McGraw-Hill Education.

[41] Elahe Soltanaghaei, Akarsh Prabhakara, Artur Balanuta, Matthew Anderson, Jan M Rabaey, Swarun Kumar, and Anthony Rowe. 2021. Millimetro: mmWave retro-reflective tags for accurate, long range localization. In *Proceedings of the 27th Annual International Conference on Mobile Computing and Networking (MobiCom '21)*. 69–82.

[42] Byung Duk Song, Kyungsu Park, and Jonghoe Kim. 2018. Persistent UAV delivery logistics: MILP formulation and efficient heuristic. *Computers & Industrial Engineering* 120 (2018), 418–428.

[43] K. P. Sreevishakh and S. P. Dhanure. 2015. A review paper on automotive crash prediction and notification technologies. In *2015 International Conference on Computing Communication Control and Automation*. IEEE, 999–1002.

[44] Qinghui Tang, Sandeep K. S. Gupta, and Loren Schwiebert. 2005. BER performance analysis of an on-off keying based minimum energy coding for energy constrained wireless sensor applications. In *International Conference on Communications (ICC)*, Vol. 4. IEEE, 2734–2738.

[45] TERABEE. 2022. Long range 40m TOF sensor | Distance sensor | Level sensing. Retrieved Aug. 9, 2022 from https://www.terabee.com/shop/lidar-tof-range-finders/teraranger-evo-40m/.

[46] Dimosthenis C. Tsouros, Stamatia Bibi, and Panagiotis G. Sarigiannidis. 2019. A review on UAV-based applications for precision agriculture. *Information* 10, 11 (2019), 349.

[47] Chao Wang, Feng Lin, Tiantian Liu, Kaidi Zheng, Zhibo Wang, Zhengxiong Li, Ming-Chun Huang, Wenyao Xu, and Kui Ren. 2022. mmEve: Eavesdropping on smartphone's earpiece via COTS mmWave device. In *Proceedings of the 28th Annual International Conference on Mobile Computing and Networking (MobiCom '22)*. 338–351.

[48] Song Wang, Jingqi Huang, and Xinyu Zhang. 2020. Demystifying millimeter-wave V2X: Towards robust and efficient directional connectivity under high mobility. In *Proceedings of the 26th annual international conference on Mobile Computing and Networking (MobiCom '20)*. 677–690.

[49] Ron Weinstein. 2005. RFID: A technical overview and its application to the enterprise. *IT Professional* 7, 3 (2005), 27–33.

[50] Xieyang Xu, Yang Shen, Junrui Yang, Chenren Xu, Guobin Shen, Guojun Chen, and Yunzhe Ni. 2017. Passivevlc: Enabling practical visible light backscatter communication for battery-free IoT applications. In *Proceedings of the 23rd Annual International Conference on Mobile Computing and Networking (MobiCom '17)*. 180–192.

[51] YIC. 2022. GPS & GLONASS receiver. Retrieved Aug. 9, 2022 from https://www.yic.com.tw/wp-content/uploads/2020/11/YIC-GU-902GG-GU-902MGG.pdf.

[52] Yeo-Sun Yoon and Moeness G. Amin. 2008. High-resolution through-the-wall radar imaging using beamspace MUSIC. *IEEE Transactions on Antennas and Propagation* 56, 6 (2008), 1763–1774.

[53] Ermao Zhao, Fangzheng Zhang, Daocheng Zhang, and Shilong Pan. 2019. Three-dimensional multiple signal classification (3D-MUSIC) for super-resolution FMCW radar detection. In *2019 IEEE MTT-S International Wireless Symposium (IWS)*. IEEE, 1–3.

[54] Renjie Zhao, Timothy Woodford, Teng Wei, Kun Qian, and Xinyu Zhang. 2020. M-cube: A millimeter-wave massive MIMO software radio. In *Proceedings of the 26th Annual International Conference on Mobile Computing and Networking (MobiCom '20)*. 1–14.

[55] Zhen-wei Zhao, Ming-gao Zhang, and Zhen-sen Wu. 2001. Analytic specific attenuation model for rain for use in prediction methods. *International Journal of Infrared and Millimeter Waves* 22, 1 (2001), 113–120.

[56] Mohammad Zomorrodi and Nemai Chandra Karmakar. 2016. Optimized MIMO-SAR technique for fast EM-imaging of chipless RFID system. *IEEE Transactions on Microwave Theory and Techniques* 65, 2 (2016), 661–669.